nature synthesis

Article

https://doi.org/10.1038/s44160-024-00669-4

Anomalous in-plane electrical anisotropy in elemental metal nanosheets

Received: 27 January 2024

Accepted: 20 September 2024

Published online: 31 October 2024

Check for updates

Taehoon Kim[1,2,10], Dongchul Seo[1,2,3,10], Sungsoon Kim[1,2,10], Gyu Won Kim[1,2], Seung-Jae Shin[4], Se Young Kim[5], Minwoo Lee[1,2], Jihong Bae[1,2], Hansol Ra[1,2], Minjun Kim[1,2], Taeyoung Kim[1,2], Soyeon Lee[1], Seung-Rok Kim[1], Hyunmin Cho[6], Han Joo Lee[6], Jaehyeok Choi[1,2], Seongil Im[6], Jin-Woo Park[1], Jinwoo Cheon[3,7,8], Joon Sang Lee[5], Aron Walsh[9] & Wooyoung Shim[1,2,3,8]

Two-dimensional (2D) elemental metals, often overlooked owing to their lack of switching or dielectric properties, have the potential to exhibit unique properties unachievable by their bulk counterparts if their microstructure can be controlled. Here we propose an electrodeposition method that utilizes a confined 2D template to prepare elemental metal nanosheets with an aligned grain orientation, resulting in an exceptionally high in-plane electrical anisotropy of >10^3. Heterogeneous nucleation is initiated and the directed growth of the metal at the cathode is controlled within a channel whose size is smaller than the critical size of the nuclei. This leads to the formation of anisotropic microstructures, and consequently, the nanosheets exhibit anisotropic electrical properties. Unlike conventional field-effect transistors, devices employing a channel with two orthogonally separated conduction paths yield an exceptional on–off switching ratio exceeding 10^4. Our approach offers a promising route to produce various 2D elemental metals with properties different from those observed in their bulk counterparts and highlights the potential of anisotropic metallic nanosheets as switching elements.

The degree of anisotropy in a material is often related to its crystal symmetry[1–9], with more symmetrical structures, such as cubic metals, typically exhibiting lower anisotropy[10–12] (Extended Data Fig. 1 and Supplementary Table 1). Therefore, the degree of electrical anisotropy in common metals is generally low. For example, Cu, a common cubic metal with a face-centred cubic (FCC) crystal structure, has an isotropic (~1) electrical conductivity in its bulk form. However, thin films of Cu can exhibit innegligible anisotropy along the out-of-plane (x–z plane) direction owing to their internal microstructure[13], with reported anisotropy ratios of up to 1.77. As the crystal structure is largely determined by free energy and may not be easily modified, microstructure control[14–16], particularly in the form of grain orientation and texture, is a key strategy for achieving anisotropic behaviour in metals.

The nucleation free energies of metals are lower than those of semiconductor materials composed of covalent bonds[17]. Consequently, metals often undergo extensive nucleation, leading to the formation of polycrystalline phases. The control of crystal grain size and orientation plays a crucial role in tailoring the electrical and mechanical properties of materials[18–22]. This manipulation can be achieved by controlling the nucleation and growth processes. Electrodeposition initiates nucleation at a specific location[23–25] (Supplementary Table 2), with the cathode serving as the energetically favoured site for the reduction of

[1]Department of Materials Science and Engineering, Yonsei University, Seoul, Korea. [2]Center for Multi-Dimensional Materials, Yonsei University, Seoul, Korea. [3]Yonsei IBS Institute, Yonsei University, Seoul, Korea. [4]School of Energy and Chemical Engineering, Ulsan National Institute of Science and Technology, Ulsan, Korea. [5]Department of Mechanical Engineering, Yonsei University, Seoul, Korea. [6]Department of Physics, Yonsei University, Seoul, Korea. [7]Department of Chemistry, Yonsei University, Seoul, Korea. [8]Center for Nanomedicine, Institute for Basic Science, Seoul, Korea. [9]Department of Materials, Imperial College London, London, UK. [10]These authors contributed equally: Taehoon Kim, Dongchul Seo, Sungsoon Kim. e-mail: wshim@yonsei.ac.kr

metal ions[26]. When this process is conducted on a flat conducting substrate, the random nucleation and growth of metal nanoparticles and nanosheets with random orientations are observed[27–29] (Fig. 1a, left). By contrast, template-mediated electrodeposition holds promise for the growth of metals into corresponding nanostructures[30–33]. However, the microstructures obtained through this method often exhibit randomly oriented grains, akin to their bulk counterparts, leading to electrical properties similar to those of bulk materials.

In this study, we propose an electrodeposition method for synthesizing 2D elemental metal nanosheets with an aligned grain orientation (right, Fig. 1a), resulting in high in-plane electrical anisotropies of over three orders of magnitude (Extended Data Fig. 1). Our method relies on a confined 2D template to direct the heterogeneous nucleation and growth of metal atoms at the cathode within a channel several angstroms in size. Importantly, this channel size is smaller than the critical nuclei size, leading to the formation of anisotropic microstructures that contribute to the observed anisotropic electrical properties. We introduce a three-terminal switching device that exhibits an on–off switching ratio exceeding 10^4. The key innovation lies in the anisotropic metal channel with aligned grain boundaries, which enables a distinct electrical conductivity in both the longitudinal and transverse directions. Further, we describe the growth mechanism and resulting characteristics of our 2D metals, followed by a demonstration of their anisotropic structure and properties.

Results

Metal deposition mechanism in 2D channel

During electrodeposition, there are two types of nucleation mechanisms: (1) heterogeneous nucleation at the cathode–electrolyte interface and (2) homogeneous nucleation within the channels. The free energy of heterogeneous nucleation[34] is a product of the free energy of homogeneous nucleation and a function of the contact angle θ, given as $\Delta G^*_{r,\mathrm{Het}} = \Delta G^*_{r,\mathrm{Hom}} f(\theta)$, where $f(\theta) = (2 - 3\cos\theta + \cos^3\theta)/4 < 1$, making nucleation more likely at the cathode. The 2D templates, unlike conventional ones[35–38], have sub-1-nm planar channels (Supplementary Note 1, Extended Data Fig. 2a and Supplementary Fig. 1). We selected a 2D template with an interlayer space ($\delta = 4.5$ Å) smaller than the critical size $2r^*$ (5.54 Å $< 2r^* <$ 11.36 Å for Ni; Supplementary Figs. 2 and 3, Supplementary Table 3 and Supplementary Note 2) at room temperature ($\delta < 2r^*$). Homogeneous nuclei have a maximum radius of $\delta/2$, which is consistently smaller than r^*, causing them to shrink and disappear (as shown by the dashed grey regions in Extended Data Fig. 2b and the grey circles in Extended Data Fig. 2c). In contrast, heterogeneous nuclei have a radius of curvature r such that $r\sin\theta = \frac{\delta}{2} < r^*$, enabling spontaneous growth when $r^* < r < r^*/\sin\theta$ (as indicated by the dashed blue lines in Extended Data Fig. 2b and the blue circles in Extended Data Fig. 2c). Within channels smaller than $2r^*$, nuclei larger than the nucleation barrier ($r > r^*$) cannot exist at the centre of the channel (homogeneous, $r_{\mathrm{homo}} < r^*$), but can form on the surface of the cathode (heterogeneous, $r_{\mathrm{hetero}} > r^*$), leading to localized nucleation and controlled grain growth.

Another critical aspect involves controlling the direction of ion diffusion. In conventional electrodeposition (Fig. 1b, top), ions diffuse ($-\mathbf{y}$) perpendicularly to the substrate (x–z plane), leading to random nucleation and isotropic crystal structures with grain boundaries in random orientations. In contrast, in 2D template-mediated electrodeposition (Fig. 1b, bottom), the template (x–y plane) aligns parallel to the ion diffusion direction ($-\mathbf{y}$). Nucleation occurs exclusively on the surface of the cathode at one end of the template, resulting in nuclei growing in one direction ($+\mathbf{y}$) towards available space. After complete growth, the grain boundaries within the sheet align uniformly, forming an anisotropic microstructure. Note that, not only the channels within the template but also the shape and position of the cathode can control the direction of ion diffusion. This could offer potential methods for achieving diverse microstructures, as intended (Supplementary Fig. 4 and Supplementary Note 1). Conventional anodic aluminium oxide templates, with pore sizes larger than $2r^*$, cannot achieve grain alignment, even when the growth direction is controlled.

To evaluate this concept, we fabricated a 2D template from graphene oxide (GO) layers confined to epoxy[39] and glass (Fig. 1c and Supplementary Fig. 5), enabling a planar channel for metal deposition via reduction. For a demonstration (Supplementary Figs. 6 and 7), we used a Watts bath for Ni deposition[40], which does not require complexing agents to maintain hydrated metal ions in the electrolyte. To explore template-mediated electrodeposition for controlling the growth direction of other metals, (1) the form and size of metal ions present in the plating bath and (2) the chemical stability between the electroplating bath and the template (Supplementary Note 3) must be considered. Note that pristine GO expands in an aqueous solution because the hydrophilic surface attracts water molecules into the layers, resulting in the hydration of the GO layers. This is due to the occurrence of van der Waals bonding, which is relatively weak compared with the strong hydrogen bonding that occurs in an aqueous solution. To maintain the interlayer space, which enables heterogeneous nucleation and suppresses homogeneous nucleation, a pair of glasses and epoxy were used to fix the interlayer spacing in the aqueous solution. The X-ray diffraction (XRD) patterns of pristine GO in the aqueous solution showed apparent time-dependent variations in peaks: (1) low-angle shifts occurred owing to an increase in the interlayer distance beyond 7.6 Å and (2) peak broadening occurred owing to sequential increases in the interlayer distance (or separation) (Fig. 1d,f and Supplementary Table 4). In contrast, the peaks from confined channels shifted by only 0.42°, indicating effective channel confinement with an interlayer distance (d) change of 0.29 Å (Fig. 1e,f and Supplementary Table 5). The free spacing (δ) was observed to be 4.3–4.6 Å by subtracting the GO layer thickness (3.4 Å) from d.

In a channel <1 nm wide, metal ion deposition involves critical steps (Fig. 1g and Supplementary Fig. 8). Initially, the size of hydrated metal ions in the electrolyte exceeds the GO spacing (δ) (step I). Partial dehydration enables ions to enter the confined template with an energy penalty (E_{H}) (Supplementary Fig. 9 and Supplementary Table 6) (step II). Thereafter, ions become electrostatically stabilized (E_{S}) by GO matrix

Fig. 1 | Working principle and concept of 2D template-mediated electrodeposition. a, A schematic of the electrodeposition method for producing nanostructures. The conventional flat surface (nanoparticle and isotropic nanosheet) and 2D template-mediated (anisotropic nanosheet) metal nanostructure produced via electrodeposition. The white dashed rectangles represent the in-plane orientation of the obtained nanosheets. **b**, A conceptual illustration for a comparison of conventional deposition and 2D template-mediated electrodeposition. **c**, A photograph of a gap-confined GO template using a pair of glasses and epoxy. The scale bar indicates 1 cm. **d**–**f**, The stable gap fixation performance of physically confined templates. XRD patterns of pristine (**d**) and gap-confined (**e**) GO wetted with deionized water, and the d spacing (**f**) of GO with respect to wetting time calculated using Bragg's law. **g**, A schematic and energy profile of a metal ion entering the gap-confined GO. Sequence of steps illustrating the interaction of hydrated metal ions with GO during 2D template-mediated electrodeposition: hydrated metal ions larger than the GO gap (δ) in the electrolyte (step I), partial dehydration enables ions to penetrate the confined GO template (step II), subsequent electrostatic stabilization of ions by functional groups on GO (such as –OH, C=O and –COOH) (step III), the release of ions from GO template interaction, allowing diffusion towards the cathode (step IV), and the reduction of diffused metal ions by electrons from the cathode surface (step V). **h**, Snapshots from MD simulations showing Ni^{2+} entering the GO channel. C atoms in the GO sheets are depicted as black spheres, O as grey spheres, H as mint spheres and Ni^{2+} as blue spheres. **i**, The simulated energy profile of Ni^{2+} entering the gap-confined GO, corresponding to the grey dashed box region in **g**. The gradient of the energy change undergoes reversal each time dehydration (positive), stabilization (negative) and diffusion (positive) occur.

https://doi.org/10.1038/s44160-024-00669-4

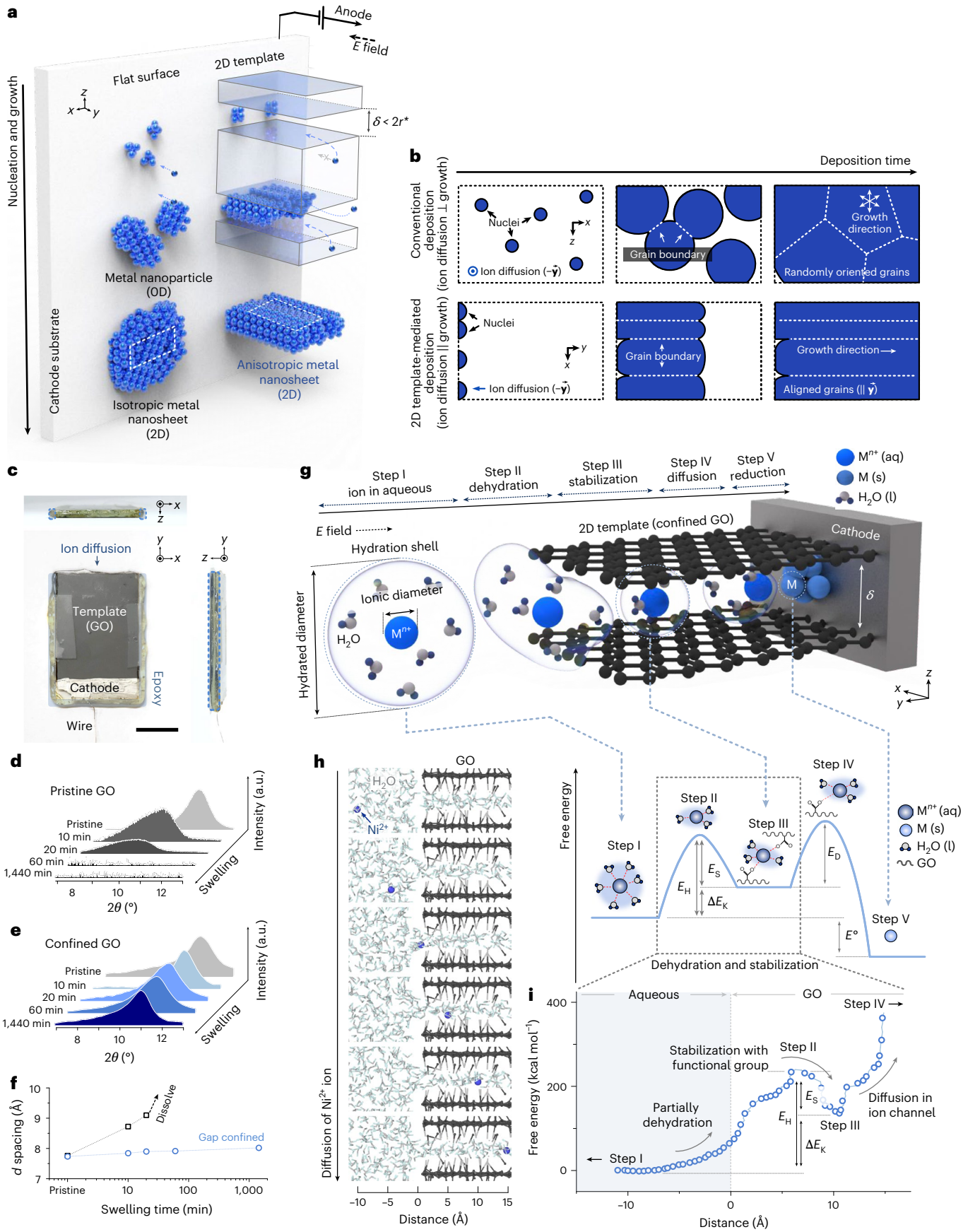

https://doi.org/10.1038/s44160-024-00669-4

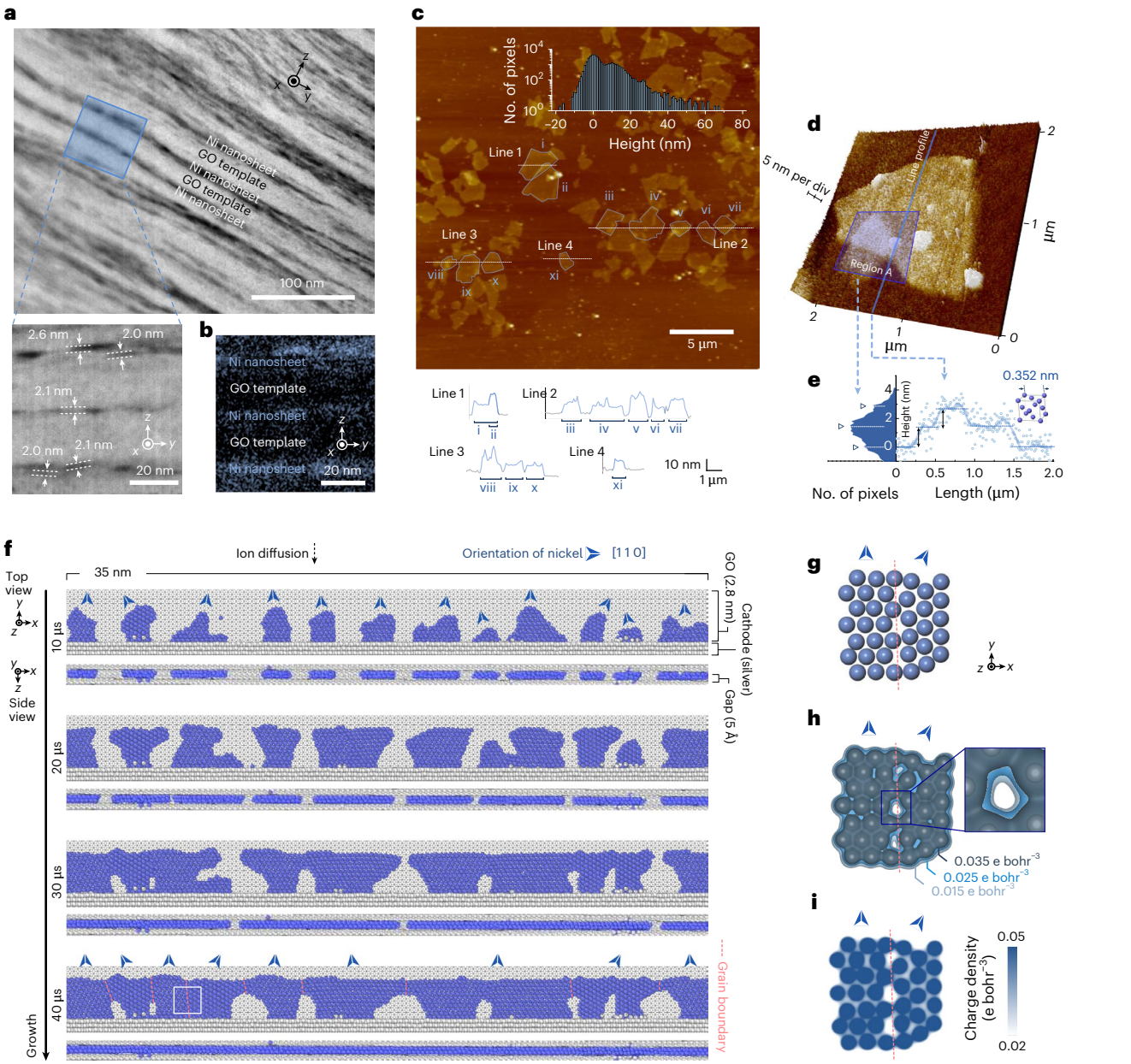

Fig. 2 | Structural characterization of 2D template-mediated Ni nanosheets. **a**, Annular BF-STEM images of the GO-based template after the electrodeposition of Ni. **b**, The magnified EDS mapping of Ni for the GO-based template after the electrodeposition of Ni. **c**, An AFM image of bulk-transferred Ni nanosheets on a SiO_2 substrate (top inset graph) with the height distribution histogram of the AFM image (bottom inset graphs). Line profiles of the bulk-transferred Ni nanosheets transferred to a SiO_2 substrate, corresponding to the white lines in the AFM image are shown. **d**, An AFM image of single 2D template-mediated Ni nanosheets on a SiO_2 substrate. The scale for height is 5 nm per division (div). **e**, Height distribution histogram and line profile of a 2D template-mediated Ni nanosheet transferred to a SiO_2 substrate, corresponding to the regions highlighted with the blue box and blue line in **d**, respectively. **f**, Simulation of Ni growth in a GO template with an interlayer gap of 5 Å shows the Ni nuclei growing from the cathode surface. The grain orientation (the blue arrowheads indicate the [1 1 0] direction) determined in the initial nucleation stage is maintained, and the grain boundaries (indicated by dashed pink lines) are parallel to the ion diffusion direction. Ni atoms are depicted as blue spheres. **g**, The atomic model (12 Å × 12 Å) of one grain boundary (dashed pink line) based on a simulation snapshot, corresponding to the white dashed box region in **f**. **h**,**i**, The corresponding electron density distribution (**h**) and its cross-section (**i**) derived from DFT calculations.

(for example, –OH, C=O and –COOH) (step III). The net energy change is given by $\Delta E_K = E_H - E_S$. The ions then escape interaction with the GO template charges and diffuse to the cathode (step IV). The diffusion flux increases within the Debye length with a diffusion energy barrier (E_D) akin to ion-sieving[41]. Electrons from the cathode surface reduce the diffused metal ions (step V), further stabilizing them because of the standard reduction potential ($E°$). Molecular dynamics (MD) simulations, which track a single Ni ion (Ni^{2+}) entering the interlayer space (Fig. 1h, Supplementary Video 1 and Supplementary Fig. 10), were used to quantify these energy barriers. Simulations confirmed the dehydration and diffusion energy barriers, with diffusion being the rate-limiting step, surpassing the dehydration energy (Fig. 1i and Supplementary Note 4). The results suggest that, despite the larger size of hydrated ions in the electrolyte compared with the gap spacing (δ) of GO, the Ni^{2+} ions could undergo dehydration and enter the internal pathways of the template by the external electric field.

Freestanding metal nanosheets and simulated microstructures

We produced freestanding Ni nanosheets by depositing the metal onto a template and then removing the template (Supplementary Figs. 11 and 12). The electrodeposition process, as shown in the representative scanning electron microscopy (SEM) image, formed Ni nanosheets between the template layers (Extended Data Fig. 3a), as confirmed by energy-dispersive X-ray spectroscopy (EDS) elemental mapping (Supplementary Fig. 13). The X-ray photoelectron spectroscopy results of the pristine and Ni-filled GO showed peaks corresponding to Ni $2p_{3/2}$ and $2p_{1/2}$ (Extended Data Fig. 3b). High-angle annular dark-field and bright-field (BF) scanning transmission electron microscopy (STEM) images supported these findings, showing a uniform distribution of Ni nanosheets within the template, with an average thickness of 2.3 ± 0.3 nm (Fig. 2a and Extended Data Fig. 3c). The EDS mapping of the Ni-filled template confirmed the separation of Ni from GO without the formation of a mixed phase (Fig. 2b and Supplementary Fig. 14).

Methods for minimizing metal damage during the removal of the GO template were also investigated (Supplementary Note 5 and Supplementary Figs. 15–17). Atomic force microscopy (AFM) results revealed Ni nanosheets with the lateral dimensions of a few micrometres and the thicknesses of mostly <13 nm (Fig. 2c and Supplementary Fig. 18). The high-resolution AFM images of overlapping sheets (Fig. 2d) showed the thickness of the individual sheets to be 1.4 nm, which is four times the lattice parameter of FCC Ni (a = 0.352 nm)[42]. The thickness doubled in the overlapping region between the single-sheet areas (Fig. 2e), with the thickness distribution in 'region A' revealing 0-, 4- and 8-unit cell thicknesses of approximately 0, 1.4 and 2.8 nm, respectively. Although a number of nanosheets were observed in a stacked form (Supplementary Fig. 19), only the freestanding Ni nanosheets were selected for subsequent electrical property measurements. The average size of the observed 2D template-mediated Ni nanosheets is limited to 1.55 μm^2 owing to the non-uniformity of GO, potentially reducing the yield of metal nanosheets from a device fabrication perspective. However, using templates made with larger GO flakes for electrodeposition allows for larger Ni nanosheets in terms of lateral size to be obtained. If a continuous van der Waals gap is secured within the 2D template, it could increase both the lateral size of the metal nanosheets and the yield of the devices (Supplementary Fig. 20 and Supplementary Note 6).

Subsequently, we examined the influence of the confined 2D template on nucleation and growth during electrodeposition using MD simulations (Fig. 2f and Supplementary Video 2). The injected Ni atoms diffused by 2.8 nm within the interlayer space of 5 Å (matching gap-confined GO) of the 35-nm-wide channel (Supplementary Fig. 21) at one atom per 10 ps. These atoms crystallized into an FCC structure over 10 μs (Fig. 2f and Supplementary Fig. 22a). These crystals displayed distinct orientations ([110]; blue arrows), but maintained a fixed direction as the simulation continued for 20, 30 and 40 μs, eventually forming grain boundaries at their contact points (dashed pink line) (Fig. 2f and Supplementary Fig. 22b). The grain boundary was aligned with both the ion diffusion (−**y**) and metal sheet growth (+**y**) directions, indicating potential grain orientation control. We further explored the electrical properties using density functional theory (DFT) calculations in a 37-atom region with two grains and one grain boundary (Fig. 2g). The 3D charge-density maps (Fig. 2h) reveal electron sharing among metal atoms, which is further illustrated in the 2D charge-density images (Fig. 2i) with the presence of linear voids (grain boundaries) in the electron distribution. Additionally, the electron localization function (ELF) mapping (Supplementary Fig. 23) indicates the absence of localized electrons and confirms that the regions of electron deficiency are indeed located at the grain boundaries.

Experimental verification of electrical anisotropy

We systematically studied the electrical properties of the Ni nanosheets (Supplementary Fig. 24) using angle-resolved direct current (DC) conductance measurements to determine the electrical anisotropy from the grain boundary alignment (Supplementary Fig. 25). Using standard electron-beam lithography (EBL), we made 12 contacts around the Ni nanosheet at intervals of π/6 (Fig. 3a). The conductance ($G = \Delta I/\Delta V$) decreased from 1,265 μS at $\theta = 0$ (the blue squares indicate the maximum nanosheet conductance direction) to 968 μS at π/6, 955 μS at π/3 and 25 μS at π/2 (red triangles) before increasing to $\theta = \pi$ (Fig. 3b). The inset of Fig. 3b illustrates the conductance at various grain boundary orientations in a single nanosheet, revealing nearly a 50-fold variation in electrical conductance between the transport parallel to the grain boundary orientation ($\theta = 0$) and the transport perpendicular to the grain boundary orientation ($\theta = \pi/2$), following a sinusoidal pattern. This ability to manipulate the grain orientation and diversify the conductivity distinguishes our approach from previous studies with template pore sizes exceeding $2r^*$.

We analysed the relationship between electrical anisotropy and crystal grain orientation in cross-sectional samples with a similar thickness (35 ± 10 nm) along two perpendicular directions (Fig. 3c, blue and red boxes). These samples, prepared using focused ion beam techniques, had planes perpendicular to each other: (1) one aligned with the common z axis and the direction of maximum conductance (y–z plane; Supplementary Fig. 26) and (2) the other along the direction of minimum conductance (x–z plane), determined through angle-resolved DC conductance measurements. Transmission electron microscopy (TEM)–EDS line scan profiling (Fig. 3d) identified the substrate (Si), pristine nanosheet (Ni) and deposited electrode regions (Cr and Au). Further TEM analyses (BF-STEM and high-resolution TEM) revealed microstructural differences between the two samples. The y–z plane displayed the geometry and symmetry of the [0 1 1] plane of FCC Ni with a consistent periodic structure and fewer grain boundaries (Fig. 3e, left), indicating predominantly heterogeneous nucleation on the cathode surface and growth along the y direction. In contrast, the x–z plane exhibited a random grain distribution with various orientations (Fig. 3e, right), highlighting the link between the crystal grain orientation and the conductivity anisotropy.

Subsequently, we compared 'sputtered' Ni thin films with varying thicknesses (t) with template-mediated Ni nanosheets in terms of electrical anisotropy using angle-resolved conductance measurements with 12 contacts (Fig. 4a and Supplementary Fig. 27). The sputtered Ni thin films (t = 10, 20, 50 and 100 nm) exhibited a consistent conductance ($G_{max}/G_{min} = 1.57 \pm 0.33$) in all directions regardless of the thickness (Fig. 4a, left and Fig. 4b, grey circles), indicating long-range isotropic microstructures (Supplementary Fig. 28, right). In contrast, the template-mediated Ni nanosheets exhibited in-plane electrical anisotropy (Fig. 4a, right and Fig. 4b, blue squares), reflecting the anisotropic microstructures (Supplementary Fig. 28, left). Furthermore, G_{max}/G_{min} increased with decreasing thickness (Supplementary Fig. 29 and Supplementary Note 7), indicating that the grains had a larger aspect ratio when grown within the highly confined interlayer spaces of GO. Notably, an unprecedented electrical anisotropy G_{yy}/G_{xx} (= G_{max}/G_{min}) of >10^3 was exhibited by the Ni nanosheet with a thickness of ~10 nm. In the measurements of electrical anisotropy in Ni nanosheets, the direction of the applied voltage was confined to the x–y plane. As a result, anisotropy in the z direction could not be experimentally determined. However, it is expected that electron scattering in the z direction will be similar to that observed in the x direction (Supplementary Fig. 30).

To evaluate the intrinsic resistivity (ρ), we positioned four-point probe electrodes at intervals along the direction of maximum conductance ($G_{max} = G_{yy}$) for each sample (Fig. 4c and Supplementary Fig. 31). Figure 4d shows the ratios of the measured sample resistivities to the bulk Ni resistivity (ρ/ρ_{bulk}), with a reference line at $\rho/\rho_{bulk} = 1$ (purple line). The sputtered thin film exhibited ρ/ρ_{bulk} in the range of 6.4–19.2 in the in-plane direction (10 nm ≤ t ≤ 100 nm) owing to random grain boundary scattering. This behaviour is consistent for both micrometre-scale (Fig. 4d, grey-filled triangles) and centimetre-scale (Fig. 4d, unfilled triangle) lateral sizes. Conversely, the grain-aligned 2D

https://doi.org/10.1038/s44160-024-00669-4

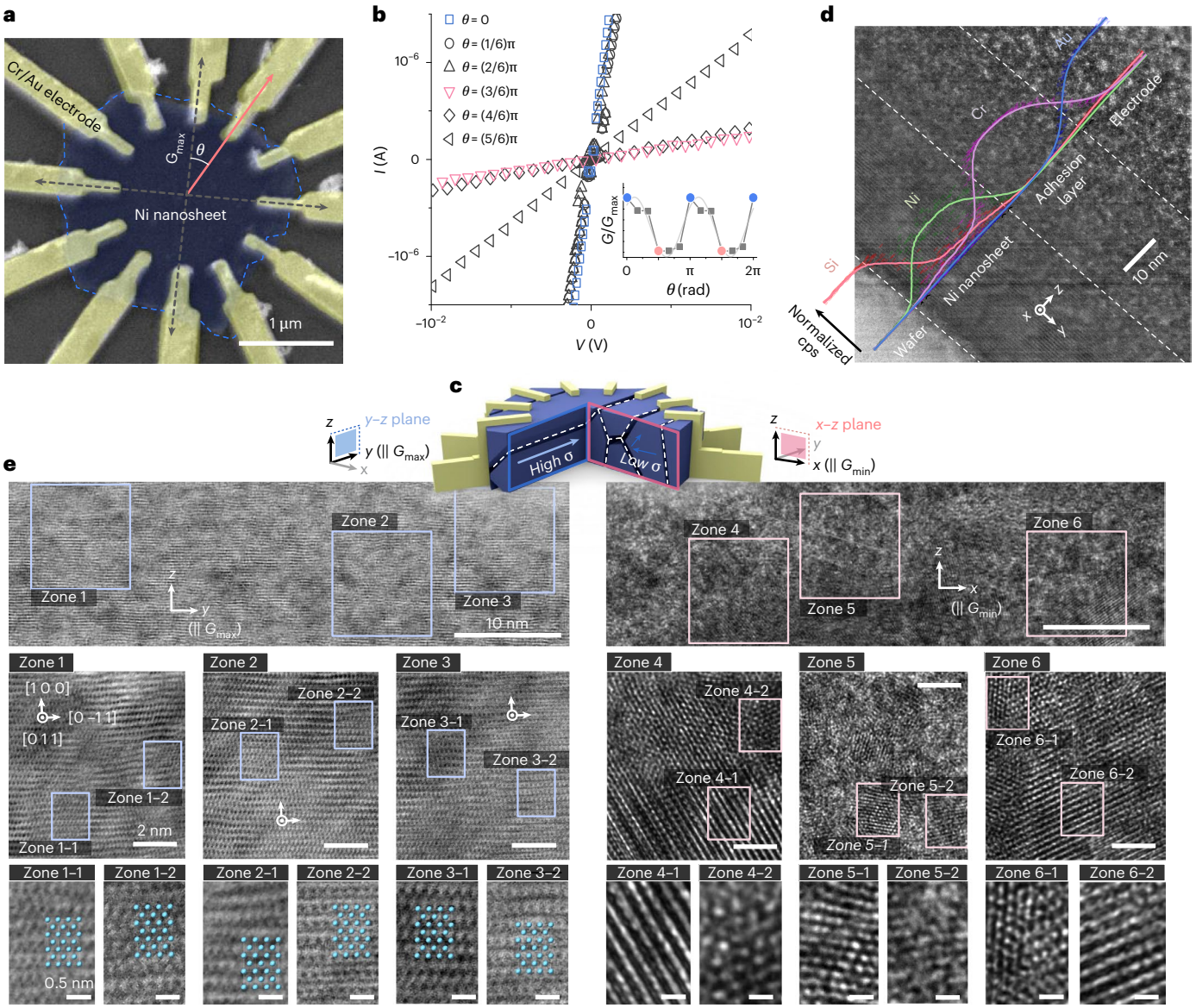

Fig. 3 | Electrical and structural anisotropy of 2D template-mediated Ni nanosheets. a, SEM image of the Ni nanosheet with 12 electrodes deposited for angle-resolved conductance measurement. The grain orientation was determined through DC conductance measurements, aligning conducting paths with the *y* axis, which minimized grain boundary scattering, maximized the electrical conductance along the *y* axis and minimized the electrical conductance along the *x* axis. **b**, *I*–*V* curve from the angle-resolved conductance measurements of the Ni nanosheet in increments of π/6 (inset). The corresponding angle-resolved conductance of the single Ni nanosheet is also shown. **c**, Schematics of the microstructures in the *y*–*z* plane (blue box) and *x*–*z* plane (red box), where G_{max} and G_{min} are respectively analysed for electrical anisotropy are shown. The white dashed lines represent the grain boundaries of the 2D template-mediated Ni nanosheets. **d**, A cross-sectional STEM image and elemental line profile (red indicates Si, green indicates Ni, purple indicates Cr and blue indicates Au) of the electrode-deposited Ni nanosheet is shown. The line profile data represents normalized counts per second (cps). **e**, Cross-sectional STEM images of the 2D template-mediated Ni nanosheet in the *y*–*z* plane (left) and *x*–*z* plane (right) observed at various magnifications.

Ni nanosheets exhibited lower ρ/ρ_{bulk} (Fig. 4d, blue circles) and longer mean free paths (Supplementary Note 8, Supplementary Fig. 32 and Supplementary Table 7) owing to the reduced grain boundary scattering, with surface scattering ($\rho_{surface}$) playing a dominant role. The correlation between the high anisotropy (G_{yy}/G_{xx}) and the grain size distribution is discussed in Supplementary Note 9 (see also Supplementary Figs. 33 and 34 and Supplementary Table 8).

Using Andrews' method[43], we derived the grain diameters (d) from the measured ratios (G_{yy}/G_{xx} and ρ/ρ_{bulk}) (Fig. 4e, triangles and squares). The grain size was validated via TEM imaging (Fig. 4e, blue-filled circles and Supplementary Fig. 35) and the full width at half maximum of the (111) peak in the XRD spectra (Fig. 4e, unfilled circles, Supplementary Fig. 36 and Supplementary Table 9). For the template-mediated Ni nanosheets, the grain size was <5 nm in the *x*–*z* direction, which was smaller than that of the sputtered thin films of equal thicknesses. TEM could not determine the grain size in the *y*–*z* direction because of the large grain sizes. However, the substantial G_{yy}/G_{xx} probably resulted from anisotropic grain sizes.

Anisotropic Ni nanosheets have shown potential for use in switching devices. A single nanosheet exhibits two resistance states. In the four-terminal orthogonal setup (Fig. 4f, inset), we cycled 12 times between the low- and high-resistance states (LRS and HRS, respectively). Uniform tenability ($I_{LRS}/I_{HRS} \cong 200$) persisted for 1,200 s, alternating V_d at 0.1 V between electrode pairs every 100 s (Fig. 4f). These Ni nanosheets demonstrated the switching potential of elemental metals as orthogonal elements.

https://doi.org/10.1038/s44160-024-00669-4

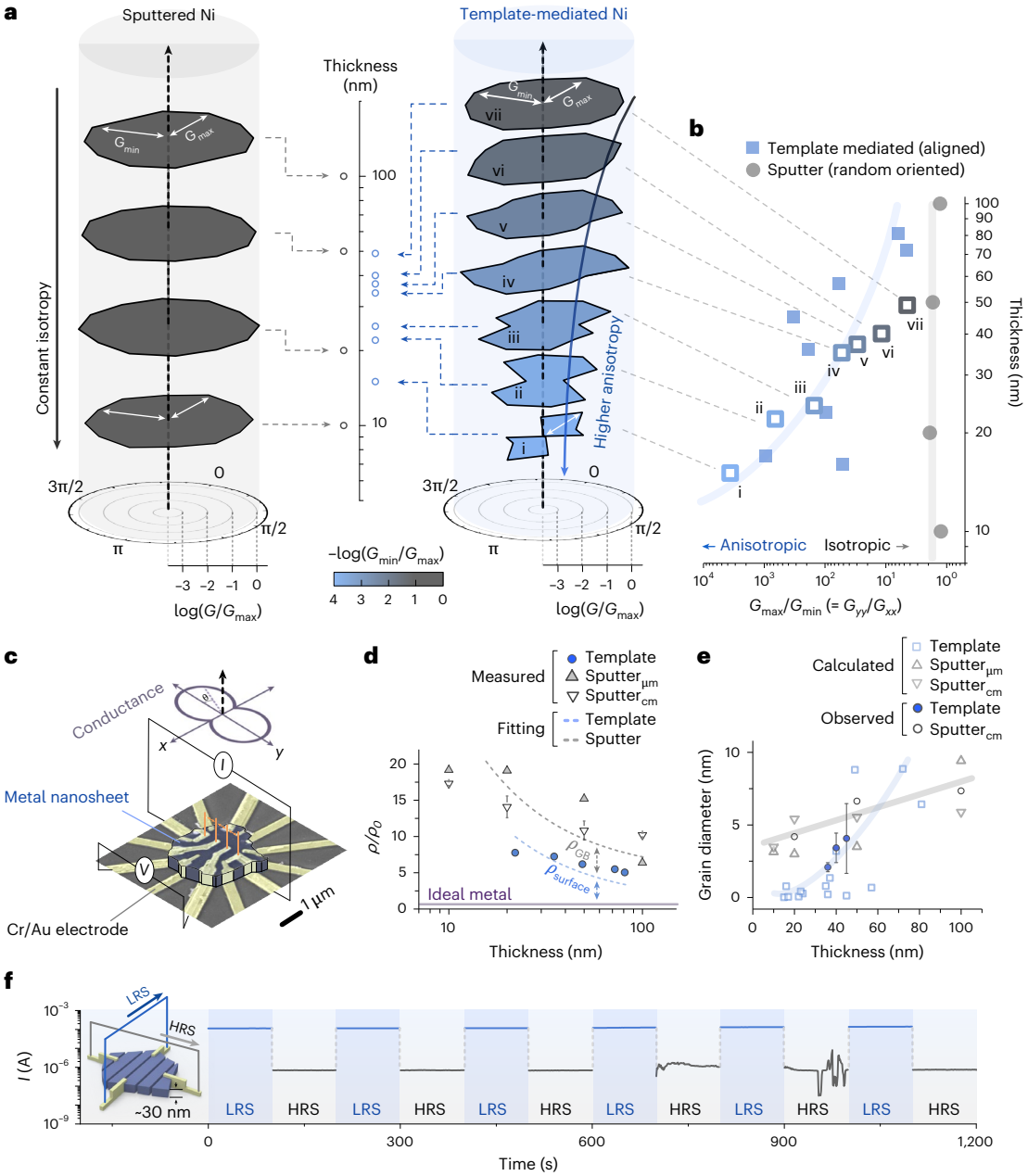

Fig. 4 | Thickness-dependent electrical properties and switching elements of 2D template-mediated Ni nanosheets. a, The thickness dependence of the angle-resolved conductance of the sputtered (grey, left) and template-mediated (blue, right) Ni nanosheets. **b**, The electrical anisotropy (G_{max}/G_{min}) of the sputtered (circles) and template-mediated (squares) Ni nanosheets as a function of the sample thickness. The unfilled squares correspond to the template-mediated Ni nanosheet samples (marked as 'i' to 'vii') shown on the right side of **a**. The shaded lines represent the trends in thickness-dependent electrical anisotropy for 2D template-mediated (blue line) and sputtered (grey line) Ni nanosheets. **c**, SEM image of four-point probe measurement in the maximum conductance ($G_{max} = G_{yy}$) direction of the nanosheets. **d**, Resistivities of the template-mediated (filled circles), sputtered with lateral size of micrometre-scale (filled triangles), sputtered with lateral size of centimetre-scale (unfilled triangles) and theoretically ideal (purple line) Ni nanosheets as a function of the thickness. Data for unfilled triangles are expressed as mean ± standard deviation from three different nanosheets ($n = 3$). ρ_{GB} and $\rho_{surface}$ represent the resistivities determined by grain boundary scattering and surface scattering, respectively. **e**, A comparison of the calculated grain diameters (open squares and triangles) with the observed grain diameters via XRD and TEM analyses (circles) for the template-mediated (unfilled squares, filled circles) and sputtered (unfilled triangles, unfilled circles) Ni nanosheets. Data for filled circles are expressed as mean ± standard deviation values from different grains in cross-section ($n = 6$, 6 and 9 for 36 nm, 40 nm and 45 nm, respectively). The shaded lines represent the trends in thickness-dependent grain diameter for 2D template-mediated (blue line) and sputtered (grey line) Ni nanosheets. **f**, The I–V curve for six sweep cycles of the 30-nm-thick Ni nanosheet switching device with an orthogonal element (left inset) exhibiting the two resistive states, the HRS (grey lines) and LRS (blue lines), at $V_d = 0.1$ V.

All-metal three-terminal electrical switch

We introduce a three-terminal switching device using single-element metals with in-plane electrical anisotropy. This all-metal device, featuring three metal electrodes, allows current modulation using an external voltage (Fig. 5a). Unlike conventional transistors, our device uses a channel with two orthogonal conduction paths ($R_{xx}/2 \gg R_{yy}/2$) (Fig. 5b, Supplementary Figs. 37–39 and Supplementary Note 10). Note that we define the voltage applied in the x direction as $V_d^{\parallel}$ and the voltage applied in the y direction as $V_d^{\perp}$. Briefly, when $V_d^{\perp} = 0$ (off state), the current measured at the source is $I_{s,off} = \frac{2V_d^{\parallel}}{R_{xx}}$. However,

https://doi.org/10.1038/s44160-024-00669-4

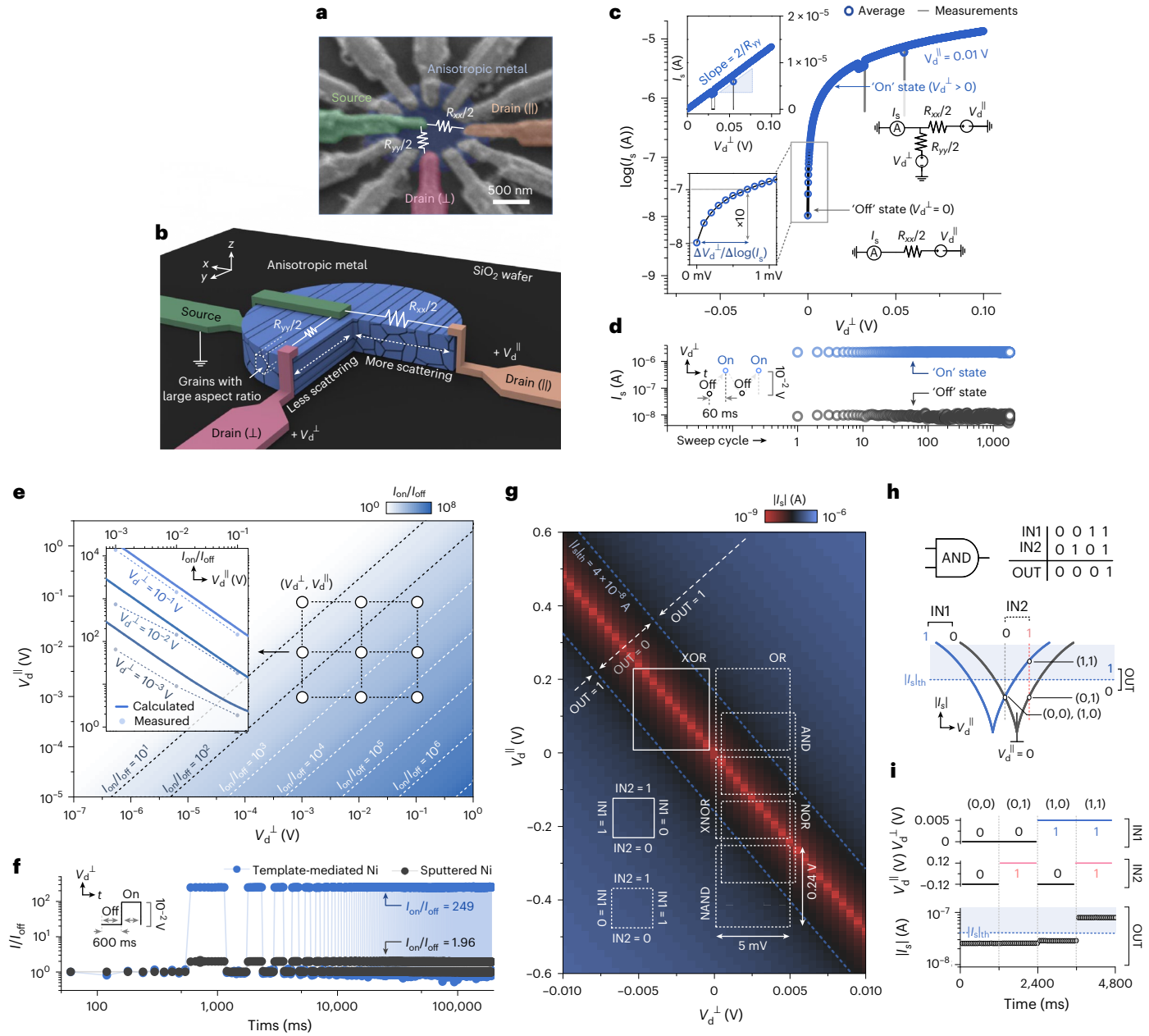

Fig. 5 | Switching properties of the all-metal three-terminal electrical switch. **a**, SEM image of the all-metal three-terminal electrical switch. **b**, The device concept of the all-metal three-terminal electrical switch. **c**, $V_d^{\perp}$-dependent transfer characterization of the all-metal three-terminal electrical switch at $V_d^{\parallel} = 0.01$ V and $V_d^{\perp} = 0$ to 10^{-1} V (top inset). The constant slope ($2/R_{yy}$) of the $V_d^{\perp}$-dependent transfer characterization is shown (bottom inset). The voltage is required to generate a one order of magnitude difference in the current ($\Delta V_d^{\perp}/\Delta\log(I_s)$) of the all-metal three-terminal electrical switch. **d**, The endurance of the current in the on ($V_d^{\perp} = 0.01$ V) and off ($V_d^{\perp} = 0$ V) states for 1,800 consecutive sweep cycles of the all-metal three-terminal electrical switch at $V_d^{\parallel} = 0.01$ V. **e**, The numerical calculation of the $V_d^{\perp}/V_d^{\parallel}$-dependent on–off ratio for an all-metal three-terminal electrical switch with an electrical anisotropy (R_{xx}/R_{yy}) of 200 (inset). A comparison between the experimental and calculated values of the on–off ratio for each combination of ($V_d^{\perp}$, $V_d^{\parallel}$) is shown. **f**, Switching behaviour of an all-metal three-terminal electrical switch based on the electrically anisotropic template-mediated and isotropic sputtered Ni nanosheets. Measurements are conducted at $V_d^{\parallel} = 0.01$ V, with switching between the off ($V_d^{\perp} = 0$ V) and on ($V_d^{\perp} = 0.01$ V) states at intervals of 600 ms. **g**, The numerical calculation of the $V_d^{\perp}/V_d^{\parallel}$-dependent $|I_s|$ for an all-metal three-terminal electrical switch with an electrical anisotropy (R_{xx}/R_{yy}) of 48.2. The four corners of the white boxes represent the input voltages ($V_d^{\perp}$, $V_d^{\parallel}$) to implement six logic gates (AND, OR, NAND, NOR, XNOR and XOR). **h**, The truth table (upper table) and schematic of output current levels ($|I_s|$) for the four input states ((IN1, IN2) = (0, 0), (0, 1), (1, 0) and (1, 1)) on the $|I_s|$–$V_d^{\parallel}$ curves (bottom graph) of the AND gate. **i**, The logic input (IN1, IN2) (upper two graphs) and measured output current levels ($|I_s|$) (bottom graph) for the logic behaviours of the AND gate. The four continuously changing (IN1 and IN2) states ((0, 0), (0, 1), (1, 0) and (1, 1)) have 20 measurements each with intervals of 60 ms, for a total of 4,800 ms.

when $V_d^{\perp} > 0$ (on state), the current measured at the source is $I_{s,on} = \frac{2V_d^{\parallel}}{R_{xx}} + \frac{2V_d^{\perp}}{R_{yy}}$, indicating a linear increase (slope: $2/R_{yy}$) (Fig. 5c, top inset graph). Consequently, the on–off ratio is $I_{s,on}/I_{s,off} = 1 + \frac{R_{xx}V_d^{\perp}}{R_{yy}V_d^{\parallel}}$, indicating that the on–off ratio of the three-terminal switching device depends on the electrical anisotropy of the metal nanosheet (R_{xx}/R_{yy}) and the ratio of the drain driving voltages ($V_d^{\perp}/V_d^{\parallel}$) (Fig. 5c).

To validate the behaviour of our three-terminal switching device experimentally, we used a 24-nm-thick Ni nanosheet with $V_d^{\parallel} = 0.01$ V. We cycled $V_d^{\perp}$ on and off in 60 ms cycles and measured I_s (Fig. 5d).

At $V_d^{\perp} = 0$ V (grey dots), I_s was 8.47×10^{-9} A, indicating electron flow with $R_{xx}/2 = 1.18 \times 10^6$ Ω. When $V_d^{\perp} = 0.01$ V was applied (blue dots), I_s increased to 2.25×10^{-6} A (2.65×10^2 times larger than that in the off state), resulting in an on–off ratio exceeding 10^2.

A higher $V_d^{\perp}$ and lower $V_d^{\parallel}$ were expected to yield a greater on–off ratio. Predictions for a metal nanosheet with $R_{xx}/R_{yy} = 200$ (Fig. 5e) showed that, for $V_d^{\perp} = 1$ V and $V_d^{\parallel} = 10^{-5}$ V, the on–off ratio exceeded 10^7. The experimental confirmation included nine combinations of $V_d^{\perp}$ and $V_d^{\parallel}$ (10^{-1}, 10^{-2} and 10^{-3} V, respectively) (Fig. 5e, inset graph, Extended Data Fig. 4a,b and Supplementary Note 11), resulting in a consistent $\log(I_{on}/I_{off})$ trend, as predicted. Notably, we experimentally achieved $I_{on}/I_{off} > 10^4$ for $V_d^{\perp} = 10^{-1}$ V and $V_d^{\parallel} = 10^{-3}$ V.

Furthermore, we examined the importance of the high R_{xx}/R_{yy} ratio in our three-terminal switching device by comparing the template-mediated Ni nanosheets with isotropic Ni nanosheets (sputtered Ni; Supplementary Fig. 40) (Fig. 5f). Under $V_d^{\perp} = V_d^{\parallel} = 0.01$ V, the expected on–off ratio was $1 + (R_{xx}/R_{yy})$. The template-mediated Ni nanosheets had an average I_{on}/I_{off} of 249, indicating an R_{xx}/R_{yy} ratio of approximately 248 (Fig. 5f, blue dots). In contrast, the isotropic nanosheets from sputtering had an average I_{on}/I_{off} ratio of 1.96, indicating an R_{xx}/R_{yy} ratio of approximately 0.96 (isotropic, ~1) (Fig. 5f, black dots). The device performance depended on the nanosheet thickness, with thinner nanosheets having a higher R_{xx}/R_{yy} value (Extended Data Fig. 4c and Supplementary Fig. 41).

Operation of two-input logic gates

We performed six logical operations (AND, OR, NAND, NOR, XNOR and XOR) by adjusting the vertical drain–source voltage ($V_d^{\perp}$) and horizontal drain–source voltage ($V_d^{\parallel}$) and manipulating the current (I_s) (Fig. 5g). To elucidate: (1) we designate $V_d^{\perp}$ as input 1 (IN1), $V_d^{\parallel}$ as input 2 (IN2) and I_s as the output (OUT) (Extended Data Fig. 5a); (2) given the absence of memory retention capabilities, we represent the output I_s as $|I_s|$, effectively replacing the concept of a memory window; (3) importantly, as the channel in the nanosheet never completely turns off ($I_s \neq 0$), we define the off-current level (OUT = 0), considered as '0', as $|I_s| < 4 \times 10^{-8}$ A (Fig. 5g, region between the dotted blue lines), and the on-current level (OUT: 1) as $|I_s| > 4 \times 10^{-8}$ A (Fig. 5g, region outside the dotted blue lines).

To determine the input voltage ($V_d^{\perp}$, $V_d^{\parallel}$) required to configure the logic gates (AND, OR, NAND, NOR, XNOR and XOR), two different $|I_s|$–$V_d^{\parallel}$ curves (Extended Data Fig. 5b) obtained from two different $V_d^{\perp}$ conditions are required (detailed in Supplementary Note 12, Supplementary Fig. 42, Supplementary Tables 10 and 11 and Extended Data Fig. 5c). For instance, to configure an AND gate (Fig. 5h, bottom graph), the following steps are required. (1) Utilize two $|I_s|$–$V_d^{\parallel}$ curves for conditions 'IN1 = 0' ($V_d^{\perp} = 0$ mV, grey curve) and 'IN1 = 1' ($V_d^{\perp} = 5$ mV, navy curve). (2) Designate the intersection points of these two curves as (0, 0) and (1, 0), and determine $V_d^{\parallel}$ at this intersection as 'IN2 = 0' ($V_d^{\parallel} = -0.12$ V, dashed grey line). (3) Designate a point on another 'IN1 = 0' curve with the same $|I_s|$ values of (0, 0) and (1, 0) as (0, 1), and determine its $V_d^{\parallel}$ as 'IN2 = 1' ($V_d^{\parallel} = 0.12$ V, dashed red line). (4) Designate the intersection of the 'IN2 = 1' line and the 'IN1 = 1' curve as (1, 1). The input voltage determined through this process for the AND logic is represented by the dashed white rectangle in Fig. 5g. In this rectangle, four input conditions [(IN1, IN2) = (0, 0), (0, 1), (1, 0) and (1, 1)] are represented as the corners (Supplementary Fig. 43). For instance, the top right corner of the dashed white rectangle representing the AND gate [(IN1, IN2) = (1, 1)] exists in the 'OUT = 1' region. This indicates that, when the device operates with the input voltages 'IN1 = 1 ($V_d^{\perp} = 5$ mV)' and 'IN2 = 1 ($V_d^{\parallel} = 0.12$ V)', it has an output current of 'OUT = 1 ($|I_s| > 4 \times 10^{-8}$ A)'. The other three corners [(IN1, IN2) = (0, 0), (0, 1) and (1, 0)] exist in the 'OUT = 0' region. This signifies that, when the device operates with the remaining three input voltages [($V_d^{\perp}$, $V_d^{\parallel}$) = (0 mV, −0.12 V), (0 mV, 0.12 V), (5 mV, −0.12 V)], it has an output current of 'OUT = 0 ($|I_s| < 4 \times 10^{-8}$ A)'. The same methodology was applied to configure the remaining five logic gates (OR, NAND, NOR, XNOR and XOR); in addition, the input voltage conditions for these five logic gates are indicated in Fig. 5g using dashed white (OR, NAND, NOR and XNOR) and solid (XOR) rectangles (Extended Data Fig. 5d–h and Supplementary Note 13).

Figure 5i and Extended Data Fig. 5i–m show the measured output ($|I_s|$) for the input voltages ($V_d^{\perp}$, $V_d^{\parallel}$) of the six logic gates after the actual operation. The output data for the four input combinations [(IN1, IN2) = (0, 0), (0, 1), (1, 0) and (1, 1)] (Fig. 5i) match the truth table for the AND logic (Fig. 5h, upper table). Additionally, the output current ($|I_s|$) measured at this point is distinguished by a threshold value ($|I_s|_{th} = 4 \times 10^{-8}$ A; Fig. 5i, dashed blue line and Extended Data Fig. 5i–m). The actual operations of the remaining five logic gates (OR, NAND, NOR, XNOR and XOR) were performed similarly (Extended Data Fig. 5i–m and Supplementary Table 12). Note that these results constitute an experimental demonstration solely intended to demonstrate the on–off characteristics of anisotropic metal nanosheet-based switching devices and are not intended for direct integration into current logic architectures.

Discussion

This study demonstrated that the grain orientation of heterogeneously nucleated and grown 2D Ni metal nanosheets is dictated by the space allowed for nucleation, as spatially confined nucleation results in aligned grains. Unlike bulk Ni, these nanosheets exhibited highly anisotropic electrical properties, with G_{yy}/G_{xx} ratios greater than 10^3, and this level of anisotropy is greater than those of other 2D metals reported thus far. The application of an external voltage activated the resistance component between the source and the vertical drain, resulting in an on–off ratio exceeding 10^4. Our proposed template-mediated electrodeposition involves achieving anisotropic 2D metals through grain boundary alignment, facilitating the fabrication of electrical switching elements. This method can be expanded to various metals by reselecting combinations of electroplating baths and 2D templates. However, some challenges remain, such as (1) the enlargement of the lateral size of freestanding nanosheets when further integrated into functional devices and (2) the uniform suppression of the 2D template during deposition when fabricating monolayer-level nanosheets. Despite these limitations, there is potential for improvement through the introduction of continuous GO films or 2D templates with better crystallinity. With these issues resolved, we believe that our approach could be adapted for the preparation of several 2D metals with properties not observed in their bulk counterparts.

Methods

Preparation of 2D template

GO films were prepared by dropping a highly concentrated GO solution (5 g l^{-1}; Graphene Supermarket) onto a substrate (glass slide) until a membrane height of 20 μm was achieved for each film. The GO films were then dried at 25 °C for 24 h. A silver paste electrode and a Cu wire were attached to the end of the prepared GO membrane. An additional glass slide paired with the substrate was placed on top of the GO. Commercial epoxy (S-208, DEVCON) was added in the gap between the glass slides, including the three corners. The epoxy was then dried at 25 °C for 24 h.

Preparation of 2D template-mediated Ni nanosheet

A pure Ni plate was used as the anode, and a 2D template with confined GO was used as the cathode that was to be plated. The electrolyte was prepared by dissolving 280 g l^{-1} $NiSO_4 \cdot 6H_2O$, 40 g l^{-1} $NiCl_2 \cdot 6H_2O$ and 30 g l^{-1} H_3BO_3 in deionized water. A uniform current (0.01 A) was applied through a power supply, which provided a uniform deposition rate. The 2D templates were plated for 24 h to ensure sufficient metal formation. After electrodeposition was completed, the 2D template filled with Ni metal was transferred onto a SiO_2 wafer after mechanical exfoliation

using a tape. To remove the template, the wafer was annealed at 350 °C for thermal decomposition[44,45].

Characterization

SEM and EDS were conducted using a JSM-7001F scanning electron microscope (JEOL). XRD was performed using the Rigaku Ultima IV X-ray diffractometer with Cu–Kα (λ = 1.5418 Å) radiation (40 kV, 150 mA), and X-ray photoelectron spectroscopy was performed using the Thermo Scientific Kα spectrometer. The morphologies and thicknesses of the nanosheets were analysed using contact-mode atomic force microscopy (AFM, XE-150, Park Systems Corp.). High-resolution TEM and STEM data were obtained using JEM-2100Plus and JEM-ARM200F with a 200 kV acceleration voltage, respectively.

MD simulation for ion entrance

The simulations were performed using a large-scale atomic/molecular massively parallel simulator (LAMMPS) package. A reactive force field (ReaxFF) was used to describe the potential energy of the GO membrane. This force field is known to accurately model hydrocarbon nanostructures, considering possible bond formation, dissociation of different bond orders and charge polarization within the molecules. The interactions between GO and the atoms in the system were calculated using the Lennard–Jones potential. The Lorentz–Berthelot mixing rule was employed for the Lennard–Jones interactions between different particles. The van der Waals interactions were truncated at 1.0 nm, and the long-range electrostatic interactions were computed using the particle–particle particle–mesh algorithm. The temperature was maintained at 300 K using a Nosé–Hoover thermostat and a damping constant of 10 fs in the constant number of molecules, volume and temperature ensemble. The simulation time step was set to 1 fs, which was adequate for investigating the phenomena under the imposed conditions. An extended simple point-charge water model was used. To reduce the high-frequency vibrations of the hydrogen bonds, the SHAKE algorithm was applied to the bonds and angles of the water molecules. The system energy was first minimized using the conjugate gradient algorithm. After the systems approached equilibrium, a production run was performed for 1 ns to collect data for analysis. Post-processing was performed using an open visualization tool.

Finite element method simulation

Three-dimensional finite element method simulations were conducted using electrostatics in AC/DC module of COMSOL Multiphysics ver. 6.1 (COMSOL). Three different values of relative permittivity (ε_r) were used for the blank materials: $\varepsilon_{r,aq}$ = 80.0 for the aqueous electrolyte, $\varepsilon_{r,1D\ template}$ = 10.0 for the templates with cylindrical voids and $\varepsilon_{r,2D\ template}$ = 5.0 for the templates with cuboidal voids. Terminal and ground conditions were applied to parallel conductive plates. Electric flux streamlines represent the orientation of the electric field vector in various geometric configurations.

MD and DFT simulation for grain growth

We performed MD simulations at 300 K using a Nosé–Hoover thermostat[46] with LAMMPS[47]. Ni nucleation was performed by inserting a Ni atom at the interlayer space every 10 ps using the 'fix deposit' in LAMMPS. The Ag cathode was modelled as four-layered FCC Ag terminated with (111) direction, and the Ag and Ni atoms were described using an EAM force field[48]. The GO templates were simply described as graphite, which had no specific interactions with Ni or Ag, and were fixed during the MD simulation. The simulation cell size was 35.1 × 8 × 6.1 nm, with 11,520 Ag atoms for the cathode and 15,744 C atoms for the template (see Supplementary Fig. 21 for details).

DFT calculations were performed using VASP[49] 5.4.4 with projector augmented-wave pseudopotentials. The Perdew–Burke–Ernzerhof[50] exchange-correlation functional and the kinetic energy cut-off of the plane-wave basis were set to 450 eV. Γ-centred (1 × 1 × 1) mesh was used to sample the reciprocal space of the isolated cluster. An additional ~15-Å thick vacuum regimen was introduced in the x, y and z directions. The convergence of the self-consistent field was set to 10^{-6} eV, and the ionic position was fixed as a snapshot from the MD simulations. The 3D charge density and localization function map was obtained using VESTA[51].

Preparation of sputtered Ni nanosheet

The sputtered Ni nanosheets were fabricated using a conventional EBL process. First, a co-polymer of 8.5 % of methacrylic acid (MAA) in methyl methacrylate (MMA) (MMA(8.5)MAA EL 9, MicroChem) was spin-coated (4,000 rpm for 50 s) onto a SiO_2/Si substrate and soft-baked at 180 °C for 90 s using a hot plate. Next, polymethylmethacrylate (PMMA A5, MicroChem) was spin-coated and baked under the same conditions, resulting in the formation of a bilayer. The P(MMA-MAA)/PMMA bilayer was then exposed to an electron-beam ion lithography system (FE-SEM; JEOL-7900F) equipped with a Nanometer Pattern Generation System (NPGS) lithography attachment (gun voltage 30 kV, area dose 650 μC cm^{-2}). The development process was performed in a 1:3 mixture of methyl isobutyl ketone and isopropyl alcohol (MIBK-IPA 1:3; MicroChem) for 60 s, followed by rinsing with isopropyl alcohol. Ni nanosheets were then deposited, followed by sputtering of Ni at a slow deposition rate of 2.2 Å s^{-1} and lift-off in acetone.

Measurement of electrical property of Ni nanosheet

Angle-resolved conductance measurements were conducted with 12 contacts and a four-point probe measurement device, following the conventional EBL process. First, PMMA (A5, MicroChem) was spin-coated (4,000 rpm for 50 s) onto the transferred Ni/SiO_2/Si substrate and soft-baked at 180 °C for 90 s using a hot plate. The PMMA layer was then exposed to an electron-beam ion lithography system (FE-SEM; JEOL-7900F) equipped with an NPGS lithography attachment (gun voltage 30 kV, area dose 650 μC cm^{-2}). The development process was performed in a 1:3 mixture of methyl isobutyl ketone and isopropyl alcohol (MIBK-IPA 1:3; MicroChem) for 60 s, followed by rinsing with isopropyl alcohol. Then, the source/drain electrodes were thermal-evaporated with the metals (Cr/Au) at a slow deposition rate of 0.5 Å s^{-1}, following which the layers were lifted off in acetone. All electrical measurements, that is, angle-resolved conductance measurements with 12 contacts and the four-point probe measurement for the 2D template-mediated and sputtered Ni nanosheets, were conducted using a Keithley 4200A-SCS parameter analyser.

Measurement of switching and logic behaviours of three-terminal electrical switch

Three-terminal electrical switch measurements were conducted with source, drain and gate contacts. To achieve equivalence in the current path length between the most conductive (source-to-gate) and least conductive (source-to-drain) electrode directions, an additional conventional EBL process was employed. First, PMMA was spin-coated (4,000 rpm for 50 s) onto the 12 contacts (template-mediated and sputtered Ni nanosheets), followed by soft-baking at 180 °C for 90 s using a hot plate. The PMMA layer was then exposed to an electron-beam ion lithography system (FE-SEM; JEOL-7900F) equipped with an NPGS lithography attachment (gun voltage 30 kV, area dose 650 μC cm^{-2}). The development process was performed in a 1:3 mixture of methyl isobutyl ketone and isopropyl alcohol mixture (MIBK-IPA 1:3; MicroChem) for 60 s, followed by rinsing with isopropyl alcohol. Subsequently, the source/drain electrodes were thermally evaporated with the metals (Cr/Au) at a low deposition rate of 0.5 Å s^{-1}, after which the layers were lifted off in acetone.

All electrical measurements, that is, three-terminal measurements of the 2D template-mediated and sputtered Ni nanosheets, were performed using a semiconductor parameter analyser (Agilent 4155C) in the dark at room temperature.

Data availability

The data supporting the finding of the study are available in the Article and its Supplementary Information. Source data are provided with this paper.

References

1. Passler, N. C. et al. Hyperbolic shear polaritons in low-symmetry crystals. *Nature* **602**, 595–600 (2022).
2. Niu, S. et al. Giant optical anisotropy in a quasi-one-dimensional crystal. *Nat. Photonics* **12**, 392–396 (2018).
3. Simonov, A. & Goodwin, A. L. Designing disorder into crystalline materials. *Nat. Rev. Chem.* **4**, 657–673 (2020).
4. Paull, O. et al. Anisotropic epitaxial stabilization of a low-symmetry ferroelectric with enhanced electromechanical response. *Nat. Mater.* **21**, 74–80 (2022).
5. Du, L. et al. Engineering symmetry breaking in 2D layered materials. *Nat. Rev. Phys.* **3**, 193–206 (2021).
6. Malinowski, P. et al. Suppression of superconductivity by anisotropic strain near a nematic quantum critical point. *Nat. Phys.* **16**, 1189–1193 (2020).
7. MacNeill, D. et al. Control of spin–orbit torques through crystal symmetry in WTe_2/ferromagnet bilayers. *Nat. Phys.* **13**, 300–305 (2017).
8. Haxhimali, T., Karma, A., Gonzales, F. & Rappaz, M. Orientation selection in dendritic evolution. *Nat. Mater.* **5**, 660–664 (2006).
9. Chu, J.-H. et al. In-plane resistivity anisotropy in an underdoped iron arsenide superconductor. *Science* **329**, 824–826 (2010).
10. Sharma, A., Gambino, R. J. & Sampath, S. Anisotropic electrical properties in thermal spray metallic coatings. *Acta Mater.* **54**, 59–65 (2006).
11. Zheng, P. & Gall, D. The anisotropic size effect of the electrical resistivity of metal thin films: tungsten. *J. Appl. Phys.* **122**, 135301 (2017).
12. Chargui, A. et al. Anisotropic thermal conductivity of nanocolumnar W thin films. *Phys. Lett. A* **426**, 127878 (2022).
13. Li, W.-Y., Li, C.-J. & Liao, H. Effect of annealing treatment on the microstructure and properties of cold-sprayed Cu coating. *J. Therm. Spray Technol.* **15**, 206–211 (2006).
14. Rivnay, J. et al. Large modulation of carrier transport by grain-boundary molecular packing and microstructure in organic thin films. *Nat. Mater.* **8**, 952–958 (2009).
15. López-Ríos, T., Briggs, A., Guillet, S., Baro, A. M. & Luna, M. Anisotropic conductivity of silver thin films grown on silicon (100) vicinal surfaces. *Appl. Phys. Lett.* **66**, 529–531 (1995).
16. Xin, G. et al. Microfluidics-enabled orientation and microstructure control of macroscopic graphene fibres. *Nat. Nanotechnol.* **14**, 168–175 (2019).
17. Rudan, M., Brunetti, R. & Reggiani, S. *Springer Handbook of Semiconductor Devices* (Springer, 2022).
18. Huang, P. Y. et al. Grains and grain boundaries in single-layer graphene atomic patchwork quilts. *Nature* **469**, 389–392 (2011).
19. Watanabe, T. & Tsurekawa, S. The control of brittleness and development of desirable mechanical properties in polycrystalline systems by grain boundary engineering. *Acta Mater.* **47**, 4171–4185 (1999).
20. Yazyev, O. V. & Chen, Y. P. Polycrystalline graphene and other two-dimensional materials. *Nat. Nanotechnol.* **9**, 755–767 (2014).
21. Yu, Q. et al. Control and characterization of individual grains and grain boundaries in graphene grown by chemical vapour deposition. *Nat. Mater.* **10**, 443–449 (2011).
22. Lin, Y., Pan, J., Zhou, H. F., Gao, H. J. & Li, Y. Mechanical properties and optimal grain size distribution profile of gradient grained nickel. *Acta Mater.* **153**, 279–289 (2018).
23. Islam, S. M., Hernandez, T. S., McGehee, M. D. & Barile, C. J. Hybrid dynamic windows using reversible metal electrodeposition and ion insertion. *Nat. Energy* **4**, 223–229 (2019).
24. Menke, E. J., Thompson, M. A., Xiang, C., Yang, L. C. & Penner, R. M. Lithographically patterned nanowire electrodeposition. *Nat. Mater.* **5**, 914–919 (2006).
25. Gamburg, Y. D. & Zangari, G. *Theory and Practice of Metal Electrodeposition* (Springer Science & Business Media, 2011).
26. Kanani, N. *Electroplating: Basic Principles, Processes and Practice* (Elsevier, 2004).
27. Martín, H. et al. Growth mode transition involving a potential-dependent isotropic to anisotropic surface atom diffusion change. gold electrodeposition on HOPG followed by STM. *Langmuir* **13**, 100–110 (1997).
28. Pötzschke, R. T., Gervasi, C. A., Vinzelberg, S., Staikov, G. & Lorenz, W. J. Nanoscale studies of Ag electrodeposition on HOPG (0001). *Electrochim. Acta* **40**, 1469–1474 (1995).
29. Gimeno, Y., Hernández Creus, A., González, S., Salvarezza, R. C. & Arvia, A. J. Preparation of 100–160-nm-sized branched palladium islands with enhanced electrocatalytic properties on HOPG. *Chem. Mater.* **13**, 1857–1864 (2001).
30. Vivas, L. G., Escrig, J., Trabada, D. G., Badini-Confalonieri, G. A. & Vázquez, M. Magnetic anisotropy in ordered textured Co nanowires. *Appl. Phys. Lett.* **100**, 252405 (2012).
31. Vivas, L. G. et al. Magnetic anisotropy in CoNi nanowire arrays: analytical calculations and experiments. *Phys. Rev. B* **85**, 035439 (2012).
32. Ozel, T., Bourret, G. R. & Mirkin, C. A. Coaxial lithography. *Nat. Nanotechnol.* **10**, 319–324 (2015).
33. Wen, L., Xu, R., Mi, Y. & Lei, Y. Multiple nanostructures based on anodized aluminium oxide templates. *Nat. Nanotechnol.* **12**, 244–250 (2017).
34. Ragone, D. V. *Thermodynamics of Materials* Vol. 2 (Wiley, 1994).
35. Taberna, P. L., Mitra, S., Poizot, P., Simon, P. & Tarascon, J.-M. High rate capabilities Fe_3O_4-based Cu nano-architectured electrodes for lithium-ion battery applications. *Nat. Mater.* **5**, 567–573 (2006).
36. Lee, J., Kim, J. & Hyeon, T. Recent progress in the synthesis of porous carbon materials. *Adv. Mater.* **18**, 2073–2094 (2006).
37. Zach, M. P., Ng, K. H. & Penner, R. M. Molybdenum nanowires by electrodeposition. *Science* **290**, 2120–2123 (2000).
38. Braun, P. V. & Wiltzius, P. Electrochemically grown photonic crystals. *Nature* **402**, 603–604 (1999).
39. Kim, S. et al. Neuromorphic van der Waals crystals for substantial energy generation. *Nat. Commun.* **12**, 47 (2021).
40. Dennis, J. K. & Such, T. E. *Nickel and Chromium Plating* (Elsevier, 1993).
41. Zhou, X. et al. Intrapore energy barriers govern ion transport and selectivity of desalination membranes. *Sci. Adv.* **6**, eabd9045 (2020).
42. Gilmore, C. *Materials Science and Engineering Properties, SI Edition* (Cengage Learning, 2014).
43. Andrews, P. V. Resistivity due to grain boundaries in pure copper. *Phys. Lett.* **19**, 558–560 (1965).
44. Jokar, E., Iraji zad, A. & Shahrokhian, S. Growth control of cobalt oxide nanoparticles on reduced graphene oxide for enhancement of electrochemical capacitance. *Int. J. Hydrog. Energy* **39**, 21068–21075 (2014).
45. Yuan, Z. et al. Sandwich-like composites of double-layer Co_3O_4 and reduced graphene oxide and their sensing properties to volatile organic compounds. *J. Alloys Compd.* **793**, 24–30 (2019).
46. Nosé, S. A unified formulation of the constant temperature molecular dynamics methods. *J. Chem. Phys.* **81**, 511–519 (1984).
47. Plimpton, S. Fast parallel algorithms for short-range molecular dynamics. *J. Comput. Phys.* **117**, 1–19 (1995).
48. Pan, Z., Borovikov, V., Mendelev, M. I. & Sansoz, F. Development of a semi-empirical potential for simulation of Ni solute segregation into grain boundaries in Ag. *Model. Simul. Mater. Sci. Eng.* **26**, 075004 (2018).

49. Kresse, G. & Furthmüller, J. Efficiency of ab-initio total energy calculations for metals and semiconductors using a plane-wave basis set. *Comput. Mater. Sci.* **6**, 15–50 (1996).
50. Perdew, J. P., Burke, K. & Ernzerhof, M. Generalized gradient approximation made simple. *Phys. Rev. Lett.* **77**, 3865–3868 (1996).
51. Momma, K. & Izumi, F. VESTA 3 for three-dimensional visualization of crystal, volumetric and morphology data. *J. Appl. Crystallogr.* **44**, 1272–1276 (2011).

Acknowledgements

This research was supported by the Nano & Material Technology Development Program through the National Research Foundation (NRF) of Korea, funded by the Ministry of Science and ICT (RS-2024-00468995) and the Yonsei University Research Fund (Post Doc. Researcher Supporting Program) in 2022 (project no. 2022-12-0140). This study was supported by a grant from the Institute for Basic Science (IBS-R026-D1).

Author contributions

Taehoon Kim, D.S., S.K. and W.S. designed the experiments. Taehoon Kim, D.S., S.K., G.W.K., M.L., J.B., H.R., M.K., Taeyoung Kim and J. Choi synthesized the materials. Taehoon.K., D.S., H.C., H.J.L., S.I. and W.S. fabricated the devices and performed the measurements. S.-J.S., S.Y.K., S.L., S.-R.K., J.-W.P., J.S.L. and A.W. performed the simulations. Taehoon Kim, D.S., S.K., G.W.K., J. Choi, J. Cheon and W.S. analysed the characteristics and performed the structural analysis. All authors wrote the manuscript and contributed to the overall scientific interpretation.

Competing interests

The authors declare no competing interests.

Additional information

Extended data is available for this paper at https://doi.org/10.1038/s44160-024-00669-4.

Supplementary information The online version contains supplementary material available at https://doi.org/10.1038/s44160-024-00669-4.

Correspondence and requests for materials should be addressed to Wooyoung Shim.

Peer review information *Nature Synthesis* thanks Teng Yang and the other, anonymous, reviewer(s) for their contribution to the peer review of this work. Primary Handling Editor: Alexandra Groves, in collaboration with the *Nature Synthesis* team.

https://doi.org/10.1038/s44160-024-00669-4

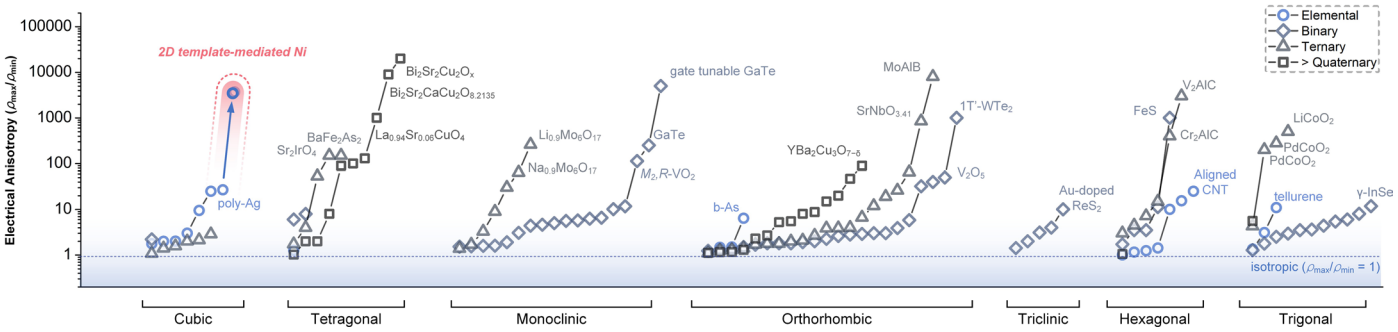

Extended Data Fig. 1 | Electrical anisotropy of existing materials. The electrical anisotropy of a material is generally determined by its atomic structure. The cubic structure, which is the most isotropic crystal system, is limited to a relatively low electrical anisotropy compared with the high anisotropy of other crystals. The greater the number of elements, the greater the possibility of anisotropy of the atomic structure. Most of the materials with higher electrical anisotropy (for example $Bi_2Sr_2Cu_2Ox$, MoAlB, V_2AlC, and GaTe) among the existing references contain three or more elements (> ternary). Ag, an elemental material with a cubic structure, exhibits high anisotropy (~27) owing to grain elongation, which suggests that microstructural control and grain orientation are related to the anisotropy of the symmetrical structure. The detailed descriptions of each data point are provided in Supplementary Table 1.

https://doi.org/10.1038/s44160-024-00669-4

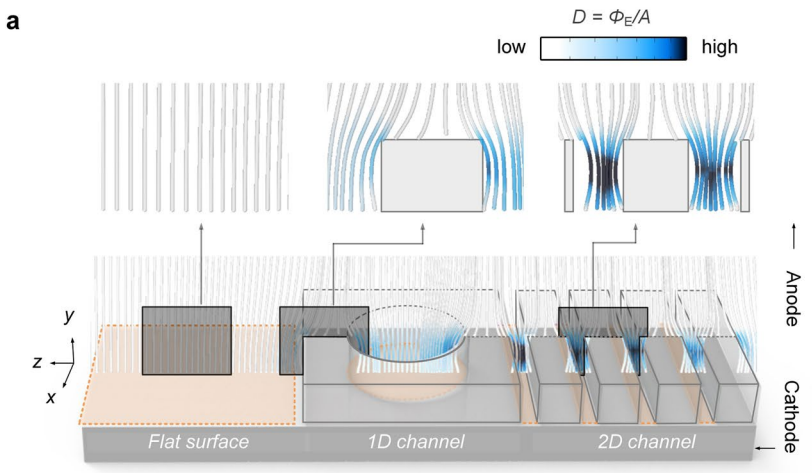

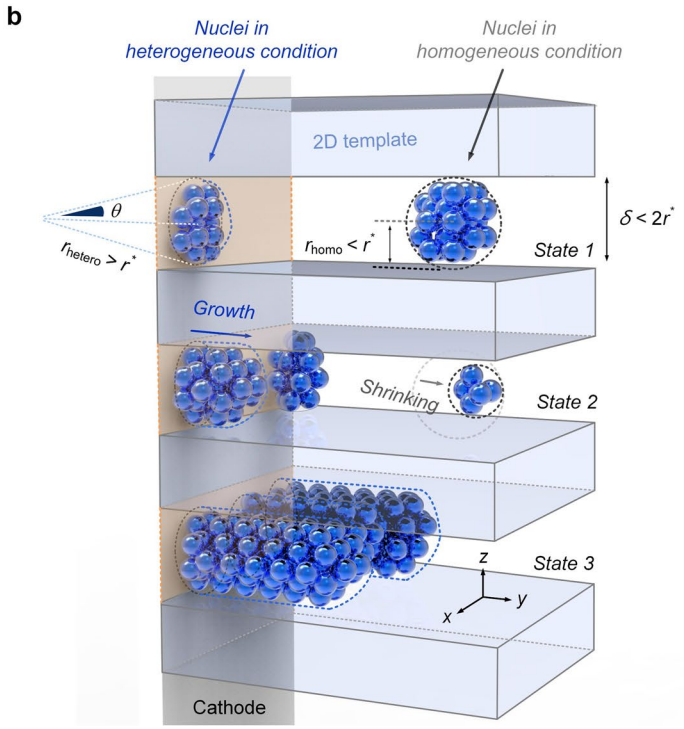

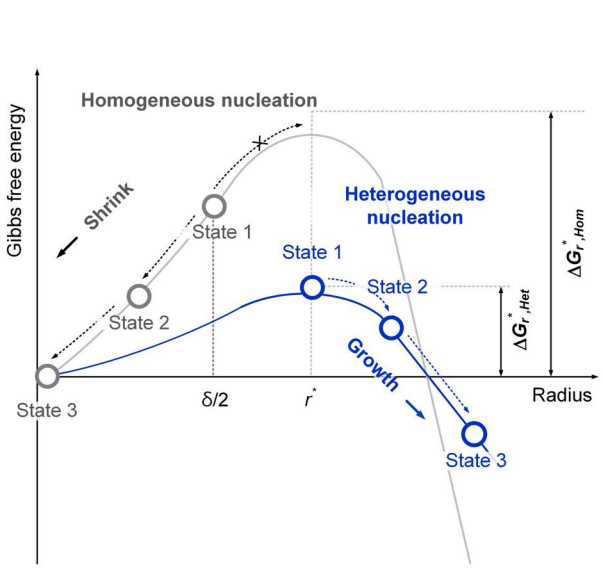

Extended Data Fig. 2 | Nucleation and growth in 2D template-mediated electrodeposition. (**a**) Distribution of electric flux (Φ_E) distorted by the template. Through the finite element method simulation results, the electric flux density D (= Φ_E/A; Φ_E: electric flux, A: area of the surface) is observed to be localized. On a flat cathode surface without a template, electric flux exists in parallel (left). The presence of a template with a lower relative permittivity than that of the surrounding medium distorts the flux at the interface between the two media, regardless of the template shape (templates with cylindrical (1D template, middle) and cuboid-shaped voids (2D template, right)). (**b**) Grain growth in the 2D template restricts the interlayer space and consequently suppresses the formation of homogeneous nuclei. Within channels with sizes smaller than $2r^*$, nuclei that surpass the energy barrier for growth cannot be formed. Only heterogeneous nuclei on the cathode surface can attain a radius of curvature greater than r^*. (**c**) Free energy as a function of the radius of homogeneous and heterogeneous nuclei. Points marked on the curves corresponding to states 1 to 3 depicted in (**b**) for homogeneous nuclei (gray open dots) and heterogeneous nuclei (blue open dots).

https://doi.org/10.1038/s44160-024-00669-4

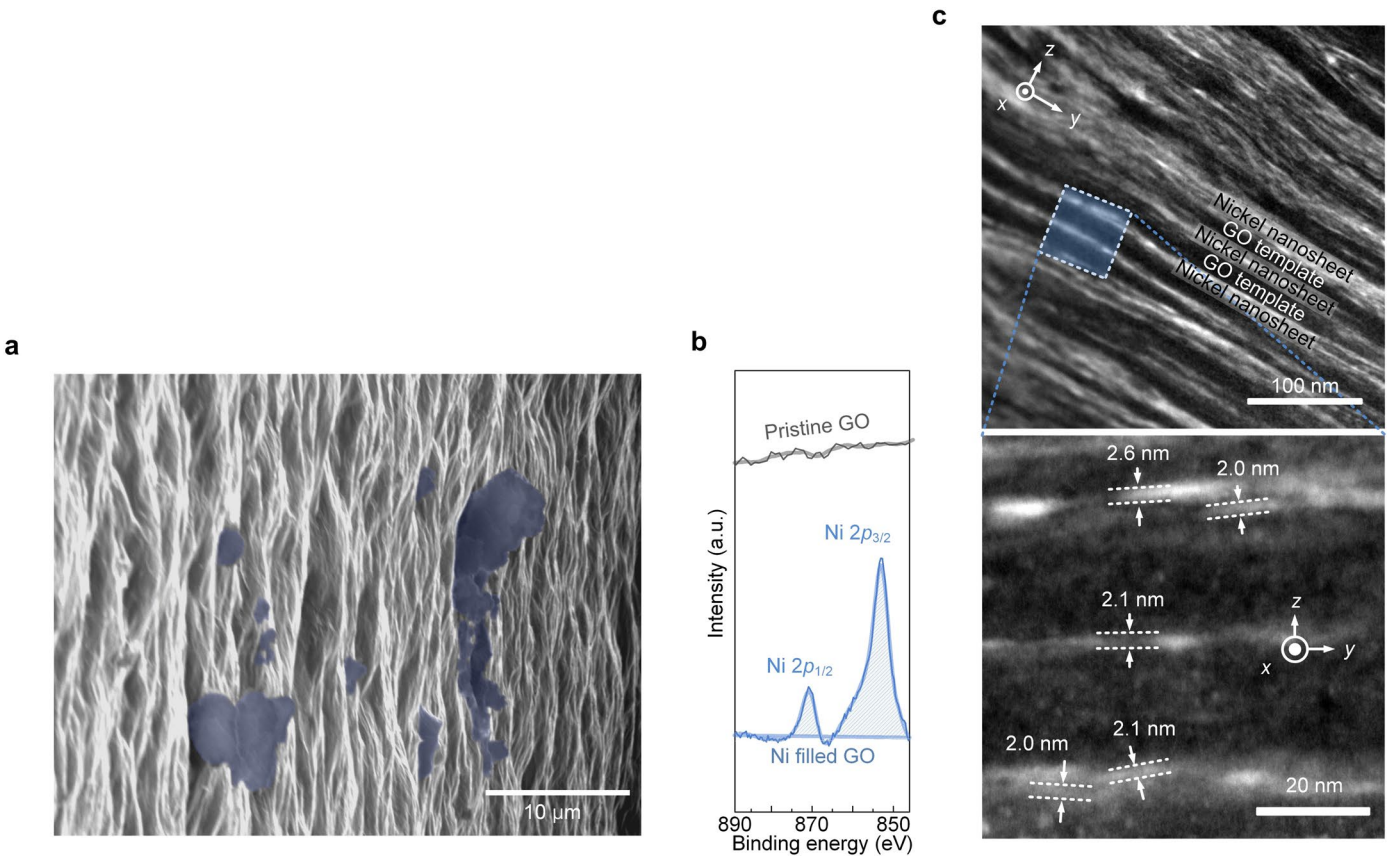

Extended Data Fig. 3 | Characterization of 2D template-mediated Ni nanosheets with the GO template. (**a**) Cross-sectional SEM image of the GO-based template obtained through cross-section polishing (CP) after electrodeposition with Ni, viewed at a tilt angle. The Ni nanosheets are highlighted in blue. (**b**) XPS spectra of the electrodeposited GO template. Spectra showing peaks corresponding to Ni $2p_{1/2}$ and $2p_{3/2}$ for the GO-based 2D template before (gray line) and after (blue line) Ni deposition. Two new peaks corresponding to Ni $2p_{3/2}$ and $2p_{1/2}$ appeared at the binding energies of 852.7 and 869.9 eV, respectively. (**c**) HAADF STEM images of the GO-based template after Ni electrodeposition.

https://doi.org/10.1038/s44160-024-00669-4

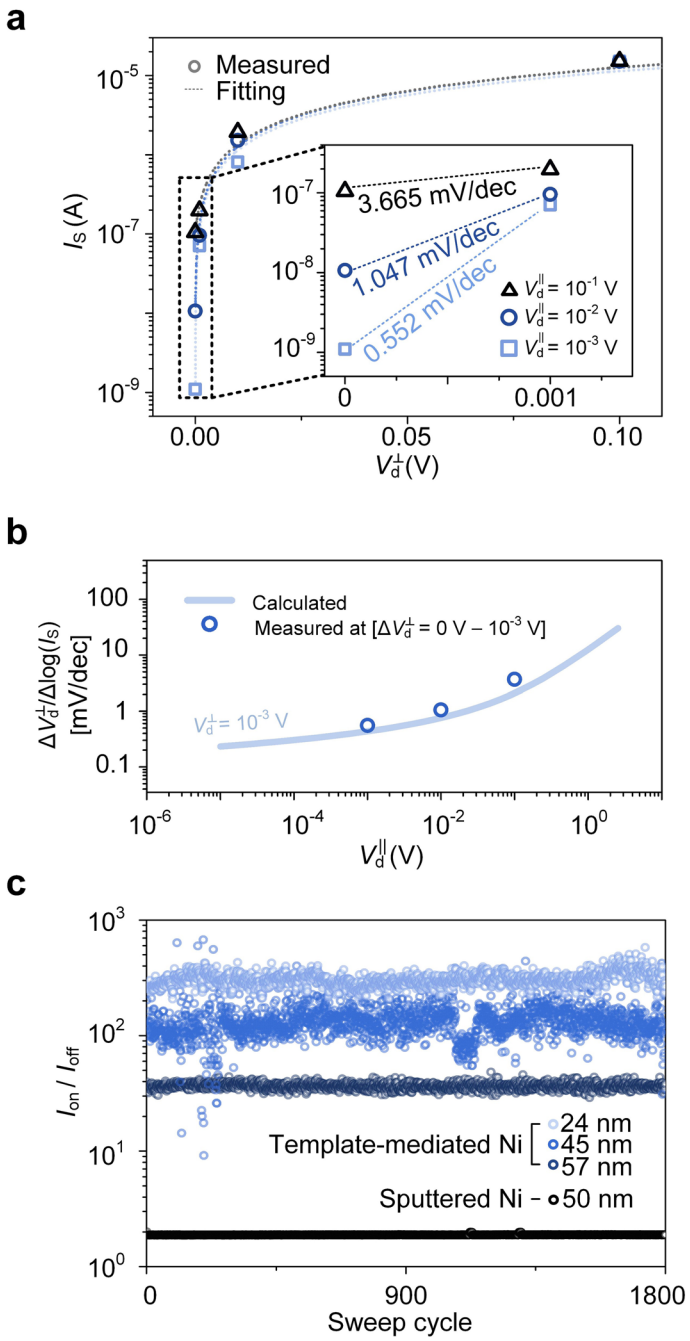

Extended Data Fig. 4 | Device performance of the all-metal three-terminal electrical switch. (**a**) Current measured from the source (I_s) for the analysis of the gate dependence of the all-metal three-terminal electrical switch using nine combinations of ($V_d^{\perp}$, $V_d^{||}$). Fitting is performed using the numerical model ($I_s = 2V_d^{||}/R_{xx} + 2V_d^{\perp}/R_{yy}$). $\Delta V_d^{\perp}/\Delta\log(I_s)$ is estimated from the slope between two measurements (between $V_d^{\perp} = 0$ V and $V_d^{\perp} = 10^{-3}$ V, inset). (**b**) Horizontal drain-voltage ($V_d^{||}$) dependence of $\Delta V_d^{\perp}/\Delta\log(I_s)$ estimated experimentally and calculated using the numerical model. The detailed descriptions of the calculated $\Delta V_d^{\perp}/\Delta\log(I_s)$ are provided in Supplementary Note 11. (**c**) On–off ratio of the all-metal three-terminal electrical switch based on the thickness-dependent electrically anisotropic template-mediated and isotropic sputtered Ni nanosheets. The measured thicknesses of the template-mediated Ni nanosheets prepared using the same method are 24, 45, and 57 nm. A 50-nm-thick isotropic sputtered Ni nanosheet has an on–off ratio of approximately 1.94. In comparison, a template-mediated Ni nanosheet with a thickness of 57 nm exhibits an on–off ratio of approximately 36.54. Reducing the thickness of the template-mediated nanosheet to 45 and 24 nm increases the on–off ratio to 139 and 286, respectively. All the measurements are performed at $V_d^{\perp} = V_d^{||} = 0.01$ V, and each measurement is performed for 1800 cycles.

https://doi.org/10.1038/s44160-024-00669-4

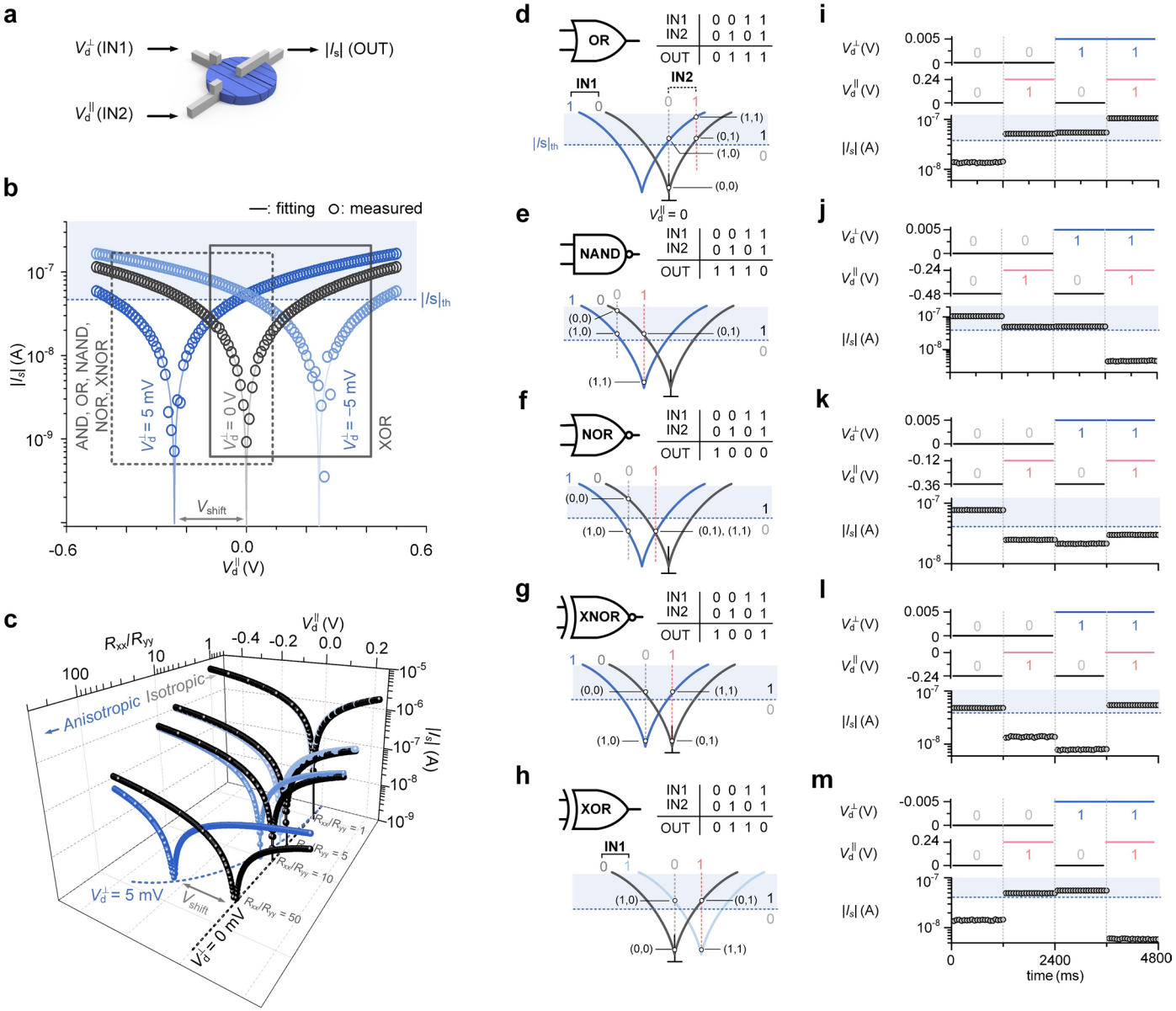

Extended Data Fig. 5 | Digital logic gates based on an all-metal three-terminal electrical switch. (**a**) Schematic of an anisotropic-metal-based three-terminal device for driving a logic gate. The device has two perpendicular input terminals (IN1($V_d^{\perp}$), IN2($V_d^{\parallel}$)) and one output terminal ($|I_s|$). (**b**) $|I_s|$–$V_d^{\parallel}$ curves for the IN1 = 0 ($V_d^{\perp}$ = 0 mV, gray curve) and IN1 = 1 ($V_d^{\perp}$ = ± 5 mV, blue curves) states. The blue dashed line indicates $|I_s|_{th} = 4\times10^{-8}$ A. (**c**) Numerical prediction of $|I_s|$–$V_d^{\parallel}$ curves with ($V_d^{\perp}$ = 5 mV) and without ($V_d^{\perp}$ = 0 V) $V_d^{\perp}$ depending on the electrical anisotropy (R_{xx}/R_{yy}). As the electrical anisotropy increases, the magnitude of the curve shift (V_{shift}) increases. The numerical approach involving variations in electrical anisotropy (R_{xx}/R_{yy}) is conducted while maintaining a constant $R_{yy} = 1.89\times10^5\,\Omega$. (**d**-**h**) Truth tables (upper table) and schematics of output current levels ($|I_s|$) for the four input states ((IN1, IN2) = (0,0), (0,1), (1,0), and (1,1)) on the $|I_s|$–$V_d^{\parallel}$ curves (bottom graph) of (**d**) OR, (**e**) NAND, (**f**) NOR, (**g**) XNOR, and (**h**) XOR gates. (**i**-**m**) Logic input (IN1, IN2) (two upper graphs) and measured output current levels ($|I_s|$) (bottom graph) for the logic behaviors of the (**i**) OR, (**j**) NAND, (**k**) NOR, (**l**) XNOR, and (**m**) XOR gates. The four continuously changing (IN1, IN2) states ((0,0), (0,1), (1,0), and (1,1)) have 20 measurements each with intervals of 60 ms, for a total of 4800 ms. The blue dashed line indicates $|I_s|_{th} = 4\times10^{-8}$ A.